Interaction of Ekman Layers and Islands

MICHAEL A. SPALL AND JOSEPH PEDLOSKY

Woods Hole Oceanographic Institution, Woods Hole, Massachusetts

(Manuscript received 21 August 2012, in final form 13 December 2012)

ABSTRACT

The circulation induced by the interaction of surface Ekman transport with an island is considered using both numerical models and linear theory. The basic response is similar to that found for the interaction of Ekman layers and an infinite boundary, namely downwelling (upwelling) in narrow boundary layers and deformation-scale baroclinic boundary layers with associated strong geostrophic flows. The presence of the island boundary, however, allows the pressure signal to propagate around the island so that the regions of upwelling and downwelling are dynamically connected. In the absence of stratification the island acts as an effective barrier to the Ekman transport. The presence of stratification supports baroclinic boundary currents that provide an advective pathway from one side of the island to the other. The resulting steady circulation is quite complex. Near the island, both geostrophic and ageostrophic velocity components are typically large. The density anomaly is maximum below the surface and, for positive wind stress, exhibits an anticyclonic phase rotation with depth (direction of Kelvin wave propagation) such that anomalously warm water can lie below regions of Ekman upwelling. The horizontal and vertical velocities exhibit similar phase changes with depth. The addition of a sloping bottom can act to shield the deep return flow from interacting with the island and providing mass transport into/out of the surface Ekman layer. In these cases, the required transport is provided by a pair of recirculation gyres that connect the narrow upwelling/downwelling boundary layers on the eastern and western sides of the island, thus directly connecting the Ekman transport across the island.

1. Introduction

Surface Ekman transport driven by wind stress parallel to a coast can drive strong boundary currents and force exchange between the coast and the basin interior, and between the upper ocean and the deep ocean. Pedlosky (1968) showed that the horizontal mass transport within a thin surface Ekman layer impinging on a vertical wall in a homogeneous ocean drives strong vertical motions in very narrow boundary layers and that they are connected to the basin-scale interior geostrophic flows. The mass flux in the Ekman layer in a stratified ocean also drives upwelling or downwelling in these narrow boundary layers near the coastal boundary and supports baroclinic boundary currents with a larger horizontal scale that is on the order of the baroclinic deformation radius (Allen 1973; Pedlosky 1974a; Gill and Clarke 1974).

Two-dimensional, linear models of these boundary currents produce very strong baroclinic flows in which the onshore/offshore flow in the surface Ekman layer is balanced by offshore/onshore flow in a bottom boundary layer. Consideration of a third dimension and spatially variable forcing allows for a more complex mass balance. Information propagates in the direction of coastal waves (coast on the right in the Northern Hemisphere), such that upstream (in a coastal wave sense) of any wind forcing the ocean will remain motionless (Gill and Clarke 1974; Allen 1976). However, as the barotropic and baroclinic pressure signals propagate downstream, strong boundary currents can develop far from the region of direct wind forcing. The mass balance in these configurations is inherently nonlocal such that there is a net offshore transport in regions of upwelling favorable winds and a net onshore transport in the regions downstream of the wind forcing (Pedlosky 1974a; Allen 1976). Friction limits the downstream distance that the wave signals propagate, but for low modes this distance is typically much larger than the baroclinic deformation radius, so very long, narrow boundary currents result. The addition of bottom topography alters the speed and structure of coastal trapped waves, and so the range of influence of wind forcing, and also reduces the role

Corresponding author address: Michael Spall, MS#21, 360 Woods Hole Road, Woods Hole, MA 02543.
E-mail: mspall@whoi.edu

DOI: 10.1175/JPO-D-12-0159.1

of the bottom boundary layer in closing the mass budget (Pedlosky 1974b; Lentz and Chapman 2004), but does not invalidate the basic conceptual model of how Ekman layers interact with coastal areas in a stratified ocean.

An interesting situation arises when the wind stress is applied along the coast of an island. If the island is sufficiently small or friction sufficiently weak, the pressure signal propagating downstream from a region of wind stress will encircle the island and arrive at the upstream side of the forcing region. A similar situation arises for wind forcing in a small enclosed sea if the pressure signal can propagate all the way around the basin perimeter. Pedlosky (1974a) showed that, for this case, the pressure on the boundary, and hence the boundary current transport, depends on a circulation integral around the basin perimeter. The circulation integral also provides a strong constraint on the circulation around islands driven by wind stress curl (e.g., Pedlosky et al. 1997). In these cases, linear quasigeostrophic models require that the integral of forcing along the island boundary be balanced by the integral of dissipation. For problems in which the net wind forcing is zero, this often requires stagnation points and multidirectional flows around the island.

We are interested in the interaction of a surface Ekman layer with the boundary of an island in a stratified ocean. We explore the weakly dissipative regime such that coastal wave signals can propagate all the way around the island in a time short compared to the viscous time scale. These results are relevant for islands smaller than this dissipation length scale and larger than the baroclinic deformation radius. In general, one could consider both the forcing by wind stress via the Ekman transport and forcing by the wind stress curl, which will provide a source of vorticity around the island. The circulation forced by wind stress curl has already been discussed extensively (e.g., Godfrey 1989; Pedlosky et al. 1997). To better isolate the effects of the Ekman layer interaction with the island boundary, we consider only cases in which the wind stress is uniform and steady. The cases discussed below are not intended to represent any particular island or region but instead identify several aspects of the oceanic response that should be pertinent to a wide range of applications.

2. Stratified, flat bottom

The circulation resulting from the interaction of a surface Ekman layer with a circular island in a stratified, flat bottom ocean is first described using a numerical model. In the following section, a complementary linear theory is developed that identifies relevant nondimensional numbers and produces circulation features that are in general agreement with the model results. Various assumptions are required to derive the analytic solution, while the numerical model introduces its own (different) approximations associated with the forcing and numerical solution technique. The general agreement in circulation and parameter dependencies provides confidence that the essential aspects of the problem are faithfully represented in both the numerical model and theory.

a. A numerical example

The numerical model used in this study is the Massachusetts Institute of Technology (MIT) general circulation model (Marshall et al. 1997), which solves the hydrostatic primitive equations on a uniform Cartesian staggered C grid with level vertical coordinates. The horizontal grid spacing is $\Delta = 5$ km, and the vertical grid spacing is 10 m. The bottom depth $D = 500$ m and flat, and the domain size is 3200 km by 3200 km. An island of 600-km radius is located in the center of the domain.[1] Calculations are carried out on a beta-plane with $f = f_0 + \beta y$, where $f_0 = 10^{-4}$ s^{-1} is the Coriolis parameter at the southern limit of the domain, $\beta = 2 \times 10^{-13}$ cm^{-1} s^{-1}, and y is distance northward. The beta effect is not very important for the behavior near the island; however, its inclusion supports barotropic Rossby waves, which facilitate the setup of the barotropic flow in the interior and the equilibrium solutions discussed below.

The model incorporates second-order vertical viscosity and diffusivity with coefficients 10^{-5} m^2 s^{-1}. The vertical diffusion is increased to 1000 m^2 s^{-1} for statically unstable conditions in order to represent vertical convection. Horizontal viscosity and diffusivity are parameterized as a second-order operator with the coefficient $A_h = 500$ m^2 s^{-1}. Temperature is advected with a third-order direct space time flux limiting scheme (MITgcm tracer advection option 33, http://mitgcm.org). Density is linearly related to temperature as $\rho = \rho_0 - \alpha_T T$, where $\alpha_T = 0.2 \times 10^{-3}$ kg m^{-3} °C^{-1} is the thermal expansion coefficient.

The model is forced at the surface with a uniform northward wind stress of 0.01 N m^{-2} for a period of three years, although the circulation is nearly steady after O(1 yr), the mixing time scale in the interior. This forcing is sufficiently weak that the resulting flow is essentially linear, allowing for more direct comparisons with the linear theory. The model is initialized with a uniform vertical stratification of $N^2 = -(g/\rho_0)\partial\rho/\partial z = (L_d f_0/D)^2$, where L_d is the baroclinic deformation radius. Temperature is also restored toward this uniform

[1] Qualtitatively similar results are found for both larger and smaller islands.

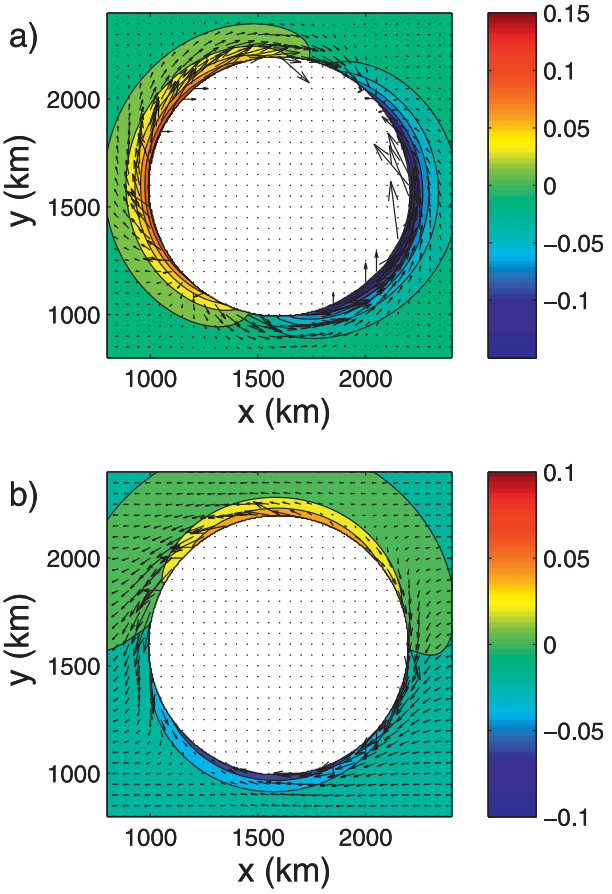

FIG. 1. Nondimensional perturbation temperature (colors, contour interval 0.02) and horizontal velocity (every tenth grid point) at (a) 25-m and (b) 195-m depth.

stratification throughout the domain with a time scale of 3×10^7 s. This allows us to isolate the island and baroclinic boundary layers from boundary effects in the finite domain and to achieve equilibrium solutions in the absence of surface buoyancy fluxes. While different in detail, this restoring fulfills the role of vertical diffusion of the density anomaly in the linear theory. The general agreement despite this difference in buoyancy mixing suggests that the circulation is not overly sensitive to details of the mixing parameterization.

An example of the steady-state circulation and temperature anomalies at 25 m and 195 m depth is shown in Fig. 1 for a case with $L_d = 30$ km. The temperature anomaly is scaled by $f_0 V \rho_0 L_d / \alpha_T g h_1$, where V is the horizontal velocity scale for the Ekman transport over the upper model level thickness $h_1 = 10$ m. The velocity away from the island is uniform and westward: this is the barotropic flow that originates at the meridional boundaries and balances the eastward Ekman transport. A much stronger velocity is generated near the island, particularly near the surface (Fig. 1a), with radial flow generally away from the island on the western side and toward the island on the eastern side. This transport downwells/upwells in a very narrow layer at the base of the Ekman layer to connect the deep interior to the surface Ekman layer. At 195-m depth (Fig. 1b) the radial velocity near the island is much weaker.

There is also a strong azimuthal velocity near the island whose phase changes with depth. This is the baroclinic flow associated with the thermal boundary layer, which is reflected in the temperature anomalies near the island. Near the surface, the western side is warm as a result of downwelling out of the surface Ekman layer and the eastern side is cold due to upwelling of dense water into the Ekman layer (Fig. 1a). This is as would be expected for the interaction of an Ekman layer with an infinite boundary. The temperature anomaly is not symmetric about the island as there is some anticyclonic phase rotation. This is quite noticeable at 195 m where the warm anomaly has shifted to the northern half of the island and the cold anomaly is to the south.

Vertical sections of the nondimensional zonal velocity (scaled by V) and nondimensional temperature anomaly are shown in Fig. 2. Near the surface, but below the thin Ekman layer, the velocity is eastward at both the northern and southern tips of the island, while below approximately 200 m the velocity is westward. This is the geostrophic flow associated with the warm and cold anomalies in the thermal boundary layer (Fig. 2b). The thermal anomalies are largest around 100-m depth and very small at the surface and bottom.[2] The circulation associated with the interaction of the Ekman layer and the island enhances the exchange from the western side to the eastern side of the island through this baroclinic flow. Because of the stratification, this also carries a positive heat flux from the western side of the island to the eastern side and may also enhance the exchange of other properties such as nutrients or passive tracers.

The pressure anomaly and the temperature anomaly within 10 km of the island are shown as a function of depth and azimuthal angle θ in Fig. 3 (zero degrees is at the eastern limit of the island). The temperature anomaly is largest at approximately 50-m depth and decays toward the bottom such that the anomalies in the deep ocean are very weak. There is a clear shift in phase in an anticyclonic direction as one moves from the surface to depth so that at some locations the sign of the

[2] This finding supports the upper and lower boundary conditions used in the linear theory below.

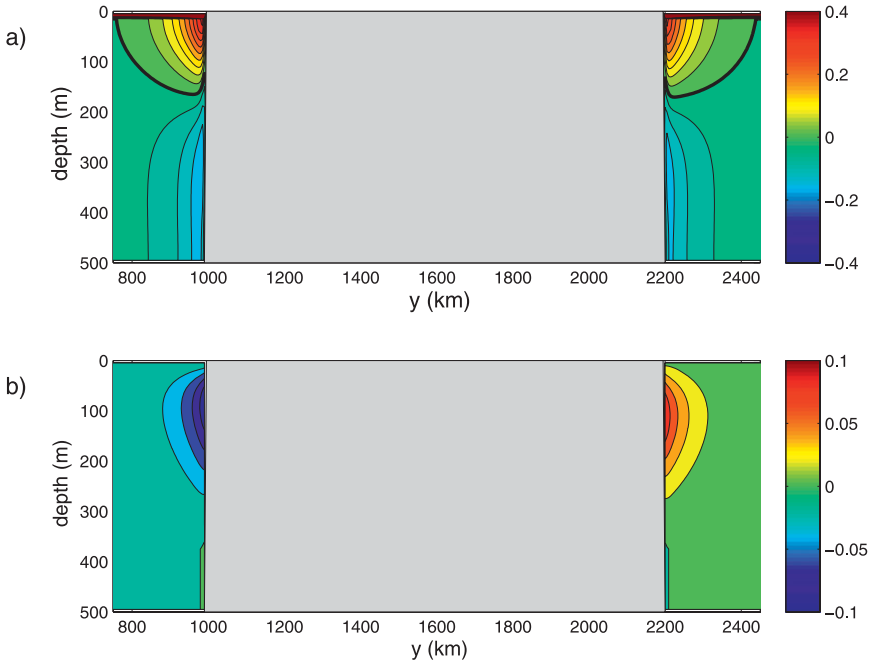

FIG. 2. Vertical section near the island at $x = 1600$ km of (a) nondimensional zonal velocity (contour interval 0.04) and (b) nondimensional temperature anomaly (contour interval 0.02).

temperature anomaly is different at depth than it is near the surface. The pressure field shows a similar structure as temperature, but it is offset cyclonically, more so at the surface than at depth, and has its maximum value at the surface. A similar anomaly structure is found for stronger stratification, but the anomalies are larger, do not penetrate as deeply, and rotate more strongly with depth.

The vertical velocity near the island (scaled by Vh_1/Δ, Fig. 3b) looks much like the temperature anomaly except with opposite sign. This reflects the essentially linear balance in the density equation, where vertical advection of the background stratification is balanced by mixing (in this case the restoring term). As a result, there are regions of vertical convergence (downwelling above upwelling along the western side of the island) and regions of vertical divergence (upwelling over downwelling along the eastern side of the island). Thus the exchange between the downwelling and upwelling boundary layers and the geostrophic interior is not uniform with depth.

The azimuthal velocity (scaled by V) also shows a complex structure around the island (Fig. 3c), with northward flow along both the eastern and western sides of the island in the upper ocean (positive tangential velocity is anticyclonic around the island). The velocity pattern rotates with depth so that the direction of flow in the deep ocean is opposite to that in the upper ocean. The depth integral of the tangential velocity is zero, but it is stronger in a relatively thin upper layer and weaker in the thicker lower layer. Since the tangential velocity is essentially geostrophic, this implies a change in sign of the horizontal temperature gradient with depth. The crest and trough in the magnitude of the azimuthal velocity that rotates anticyclonically with depth are nearly coincident with the regions of vertical mass flux convergence and divergence (the zero line in the vertical velocity is given by the white contour), providing closure for the mass balance. Finally, the radial velocity (Fig. 3d) is generally toward the boundary along the eastern side of the island (negative) and away from the boundary along the western side (positive).

b. *Linear theory*

In this section we consider a simple linear theory for the circulation induced around the island by a constant meridional wind stress. Although the linear theory requires strong approximations that are not employed in the numerical model, it nonetheless allows us to expose certain important dynamical features that seem robust across the range of models used in our study, analytical and numerical. Our nondimensional linear model is governed by the following equations, in standard polar coordinates (u, v are radial and azimuthal velocities, respectively):

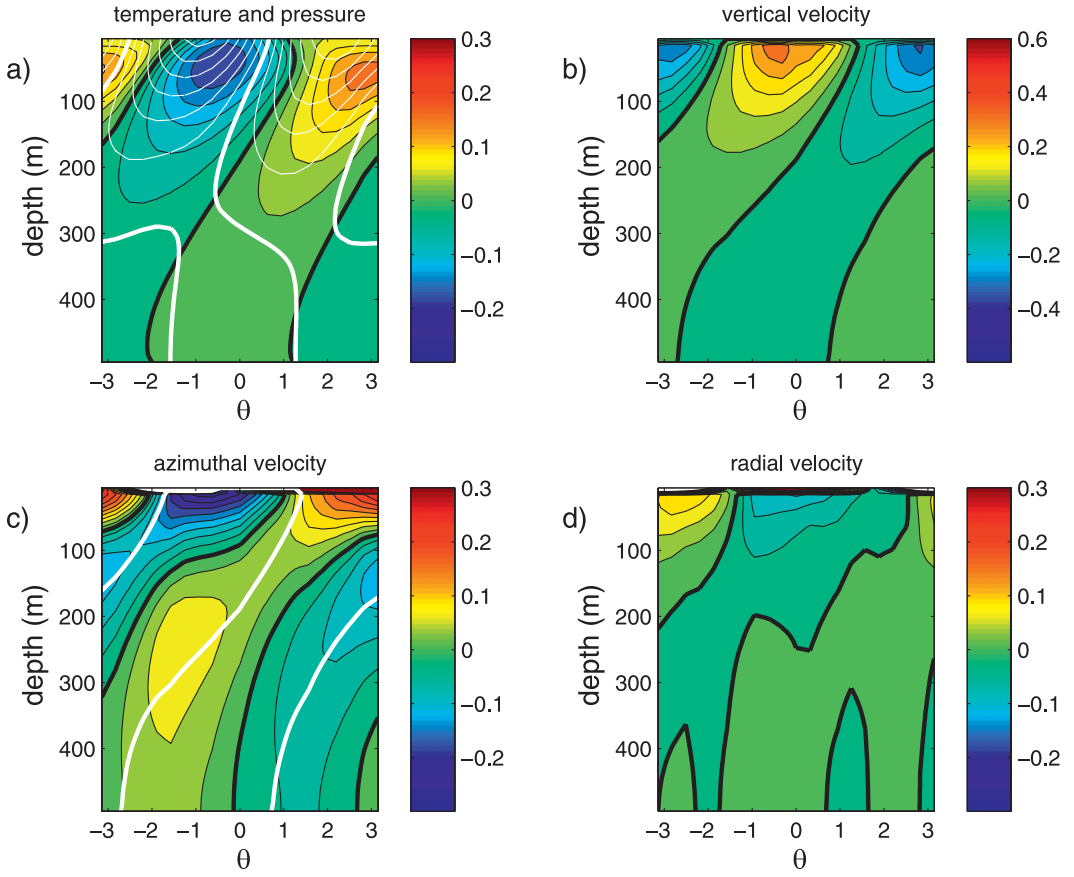

FIG. 3. Vertical section of (a) temperature anomaly (colors, contour interval 0.03) and pressure anomaly (white contours, contour interval 0.01); (b) vertical velocity (contour interval 0.06); (c) azimuthal velocity (contour interval 0.03), and (d) radial velocity (contour interval 0.03) within 10 km of the island as a function of depth and azimuthal angle. The bold black line is the zero contour in each panel; the white contour in (c) is the zero contour of the vertical velocity.

$$-fv = -\frac{\partial p}{\partial r} + \frac{E_v}{2}\frac{\partial^2 u}{\partial z^2} + \frac{E_h}{2}\left(\nabla_1^2 u - \frac{u}{r^2} - \frac{2}{r^2}\frac{\partial v}{\partial \theta}\right), \tag{1a}$$

$$fu = -\frac{1}{r}\frac{\partial p}{\partial \theta} + \frac{E_v}{2}\frac{\partial^2 v}{\partial z^2} + \frac{E_h}{2}\left(\nabla_1^2 v + \frac{2}{r^2}\frac{\partial u}{\partial \theta} - \frac{v}{r^2}\right), \tag{1b}$$

$$0 = -\frac{\partial p}{\partial z} - \rho, \tag{1c}$$

$$-wS = \frac{E_v}{2\sigma_v}\frac{\partial^2 \rho}{\partial z^2} + \frac{E_h}{2\sigma_h}\nabla_1^2 \rho, \tag{1d}$$

$$0 = \frac{1}{r}\frac{\partial (ru)}{\partial r} + \frac{1}{r}\frac{\partial v}{\partial \theta} + \frac{\partial w}{\partial z}, \tag{1e}$$

where ∇_1^2 is the horizontal Laplacian operator. The horizontal velocity component scale is

$$\frac{\tau_0/\rho}{(2A_v f_0)^{1/2}};$$

the horizontal lengths are scaled with the characteristic radius of our circular island, L, and the pressure and density anomalies are related to the velocity scale by the usual geostrophic and hydrostatic scale relations. The velocity scale is chosen so that the velocity induced in the upper Ekman layer is $O(1)$. The scale of the vertical velocity is a factor D/L smaller than that of the horizontal velocity. The parameters measuring the viscous and dissipative terms are the Ekman numbers,

$$E_v = \frac{2A_v}{f_0 D^2}, \quad E_h = \frac{2A_h}{f_0 L^2}. \tag{2}$$

In (2) A_v and A_h are the vertical and horizontal mixing coefficients of momentum. The associated Prandtl numbers σ_v and σ_h in (1d) are the ratio of the vertical and horizontal mixing coefficients of heat with respect to their momentum equivalents. The stratification parameter $S = N^2 D^2/f_0^2 L^2$, where N is the buoyancy frequency and f_0 is the dimensional value of the Coriolis parameter

at the midlatitude of our domain: in nondimensional form, $f = 1 + by$, $b = \beta L/f_0$. The thermodynamic equation (1d), originally written in terms of temperature has been rewritten in terms of the density anomaly assuming a simple linear relation between temperature and density.

Boundary conditions are as follows. On vertical boundaries, for example, $r = r_T$, the nondimensional radius of the island:

$$(u, v, w) = 0, \tag{3a}$$

$$\nabla\rho \cdot \mathbf{n} = 0. \tag{3b}$$

On the upper and lower surfaces, at $z = 1$ and 0, the density perturbation around the basic stratification is taken to be zero (recall Fig. 2):

$$\rho = 0, \quad z = 0, 1. \tag{3c}$$

The application of a uniform stress in the meridional (y) direction of nondimensional magnitude τ_0, yields a flux of fluid in the upper Ekman layer in the x direction. When it impinges on the eastern boundary of our domain, it exits into the interior below the Ekman layer as a concentrated source for the deeper geostrophic flow. That flow is absorbed in a dissipative boundary layer, and the baroclinic portion of the flow is captured in a narrow region near the boundary. The barotropic portion of that flow leaves the boundary layer and travels westward. Its nondimensional magnitude is simply $\tau E_v^{1/2}/2$: the reader may check that this yields a dimensional barotropic westward transport $\tau_0/\rho f$. The details of this calculation are not presented since the theory is essentially the same as the theory for the flow in the vicinity of the island, which is the focus of our attention and which we discuss next. The flow in the geostrophic interior, heading westward, is barotropic and is given by the pressure field; that is,

$$p_I = \frac{\tau}{2} E_v^{1/2} y. \tag{4a}$$

This corresponds the westward zonal velocity

$$u_I = -\frac{\tau}{2f} E_v^{1/2} \tag{4b}$$

and the dimensional zonal velocity, $-\tau/\rho f D$. It is the interaction of this impinging flow with the circular island that is of interest.

There are two boundary layers that we will find on the rim of the island. The structure of the boundary layers depends on the parameters in (1), and we will, for simplicity, restrict our attention to a parameter regime in which the following conditions are satisfied

$$1 \gg \delta_m = \left(\frac{E_h}{b}\right)^{1/3} \gg \delta_\lambda = \left(\frac{E_h \sigma_v}{E_v \sigma_h}\right)^{1/2} \gg \delta_h = (\sigma_h S)^{1/2}. \tag{5}$$

The scale δ_h is the scale of the hydrostatic layer (Barcilon and Pedlosky 1967), while the scale δ_λ of the wider boundary layer is the scale at which lateral diffusion of density (temperature) balances the larger vertical diffusion of density. This latter boundary layer appears in simple models of coastal upwelling, for example, Pedlosky (1974a). Indeed, much of the analysis in this section is quite similar to that earlier work, but here we focus on important structural consequences of the dynamics that were previously unexplored. The final inequality is a statement that β effects within the boundary layer structure are not important.

The boundary layers are required to represent the motion induced by the interaction of the impinging barotropic flow with the circular island. We represent the total fields as the sum of the interior field given by (4a) and *correction* fields of velocity, density, and pressure. For example, in the hydrostatic layer we represent the correction fields (indicated by carets) as

$$(u_h, v_h, w_h, p_h, \rho_h) = U_h(\hat{u}, \hat{v}/\delta_h, \hat{w}/\delta_h, \hat{p}, \hat{\rho}). \tag{6}$$

The constant U_h is to be determined in the matching procedure and the factors of δ_h display the relative magnitudes of the correction fields. The radial velocity is much weaker than the azimuthal and vertical velocities by a factor of the nondimensional boundary layer width. Introducing the boundary layer coordinate $\eta = (r - r_T)/\delta_h$, where r_T is the nondimensional radius of the island, the governing equations to lowest order become

$$f\hat{u} = -\frac{1}{r_T}\frac{\partial \hat{p}}{\partial \theta} + \frac{E_h}{2\delta_h^3}\hat{v}_{\eta\eta}, \tag{7a}$$

$$f\hat{v} = \frac{\partial \hat{p}}{\partial \eta}, \tag{7b}$$

$$\hat{\rho} = -\frac{\partial \hat{p}}{\partial z}, \tag{7c}$$

$$\hat{w} = -\frac{E_h}{2\delta_h^3}\hat{\rho}_{\eta\eta}, \tag{7d}$$

$$\hat{u}_\eta + \frac{1}{r_T}\hat{v}_\theta + \hat{w}_z = 0. \tag{7e}$$

We have used a subscript notation for some derivatives. Note that the radial velocity is not geostrophic; rather, the radial velocity has a geostrophic component given by the azimuthal derivative of the pressure and

an ageostrophic part due to the lateral momentum diffusion. Our ordering relations given in (5) do not determine their relative magnitude. In any case, a single expression for the pressure field can be easily derived. The correction pressure $\hat{p}$ satisfies

$$f^2\hat{p}_{zz} + \hat{p}_{\eta\eta} = 0. \tag{8}$$

To satisfy the condition (3c) on the density perturbation at $z = 0, 1$ we can write the solution to (8) as

$$\hat{p} = \sum_{n=1}^{\infty} P_{hn} e^{-\mu_n f \eta} \cos(\mu_n z), \quad \mu_n = n\pi. \tag{9}$$

Note that the sum begins with $n = 1$. The $n = 0$ term does not decay with distance from the boundary and is unacceptable as a boundary layer correction field, all of which must vanish as the interior is approached. Hence this layer cannot carry a barotropic correction field for the velocity. The geostrophic radial velocity is

$$\hat{u}_{\text{geos}} = -\frac{1}{r_T}\frac{\partial}{\partial\theta}\sum_{n=1}^{\infty}\frac{P_{hn}}{f}e^{-\mu_n f\eta}\cos\mu_n z, \tag{10a}$$

while the ageostrophic part of the radial correction velocity is

$$\hat{u}_{\text{ageos}} = \frac{E_h}{2(\sigma_h S)^{3/2}}\sum_{n=1}^{\infty} -P_{hn}\mu_n^3 e^{-\mu_n f\eta}\cos\mu_n z. \tag{10b}$$

The ratio of the ageostrophic to the geostrophic radial velocity will be of the order, for each term in the sum over μ_n,

$$\frac{\hat{u}_{\text{ageos}}}{\hat{u}_{\text{geos}}} = \frac{E_h\mu_n^3}{(\sigma_h S)^{3/2}} r_T \approx \frac{A_h}{f_0 L_d^2}\frac{R_T}{L_d}\mu_n^3, \tag{11}$$

after use is made of the definitions of the nondimensional parameters. The ratio, rewritten in terms of more familiar parameters in the final term on the rhs of (11), is a product of three terms. The first factor is a measure of the scale of the horizontal Ekman layer compared to the baroclinic deformation radius, normally taken to be small. The second factor represents the radial pressure gradient over the azimuthal pressure gradient and is expected to be large (R_T is the dimensional island radius). The final term is $O(1)$ but rapidly becomes large as n increases. We will need both geostrophic and ageostrophic contributions to obtain a satisfactory representation of the radial velocity in the hydrostatic layer. Note that the larger islands will tend to have a greater fraction of u that is ageostrophic while increasing the stratification enhances, relatively speaking, the geostrophic contribution.

The broader layer is a diffusion layer that exists under the conditions (5). The governing equation in the diffusion layer is a balance between the horizontal and vertical diffusion of density. Writing the pressure correction in this layer as

$$p_\lambda = U_\lambda\tilde{p}(\xi,\theta,z), \quad \xi = (r - r_T)/\delta_\lambda, \quad \delta_\lambda = \left(\frac{E_h\sigma_v}{E_v\sigma_h}\right)^{1/2}, \tag{12a}$$

$$\tilde{p}_{zz} + \tilde{p}_{\xi\xi} = 0. \tag{12b}$$

The condition that the density anomaly vanish on the upper and lower boundaries leads to a solution of (12b) in the simple form

$$\tilde{p} = \sum_{n=1}^{\infty} P_{\lambda n} e^{-\mu_n\xi}\cos\mu_n z, \tag{13}$$

where the boundary layer correction is purely baroclinic, as it was for the hydrostatic layer. The broader width of this layer implies that the radial velocity will be geostrophic, so the correction to the radial velocity will be, simply,

$$u_\lambda = -\frac{U_\lambda}{fr_T}\frac{\partial\tilde{p}}{\partial\theta}. \tag{14}$$

On the island, the effect of the wind-driven flow in the Ekman layer is to produce a concentrated source (or sink) of mass at the upper boundary of the fluid, at the rim of the cylindrical island. We represent that velocity, which drives the flow beneath the Ekman layer, as a radial sink (or source) on $r = r_T$, as

$$u(r_T,\theta,1) = -\frac{E_v^{1/2}}{2f}\tau\cos\theta\delta(z-1), \tag{15}$$

where $\delta(z - 1)$ is the Dirac delta function centered at $z = 1$. With (4a), (10a), (10b), and (14), the condition on the radial velocity at the boundary of the island becomes

$$-\frac{E_v^{1/2}}{2f}\tau\cos\theta + U_h\sum_{n=1}^{\infty}\left[-\frac{1}{r_T}\frac{\partial P_{hn}}{\partial\theta} - \frac{E_h\mu_n^3 f}{2\delta_h^3}P_{hn}\right]\cos\mu_n z - U_\lambda\sum_{n=1}^{\infty}\frac{1}{fr_T}\frac{\partial P_{\lambda n}}{\partial\theta}\cos\mu_n z = -\frac{\tau}{2f}E_v^{1/2}\cos\theta\delta(z-1); \tag{16}$$

that is, the sum of the interior zonal flow's component perpendicular to the island with the contribution from the two boundary layers must match the upwelling sink at the island's upper Ekman layer intersection with the

island perimeter. Both the interior barotropic flow normal to the island and the sink of fluid representing the flux into the upper Ekman layer impose a $\cos\theta$ dependence on the forcing in (16). Note that the combination of these terms leaves the boundary layers only a purely baroclinic net flow that must be corrected to zero. This is the qualitatively similar situation that occurs on the eastern boundary of the basin giving rise to the purely barotropic zonal flow (4b) once the boundary layers on the eastern boundary have been traversed by the fluid. The no slip condition on the island perimeter implies that

$$U_\lambda \sum_{n=1}^{\infty} P_{\lambda n}(-\mu_n/\delta_\lambda)\cos\mu_n z + U_h \sum_{n=1}^{\infty} P_{hn}(-\mu_n f/\delta_h)\cos\mu_n z = 0. \quad (17)$$

Combining (16) and (17) yields

$$p_\lambda(\xi,\theta,z) = \mathrm{Re} i\tau E_v^{1/2} r_T \times \sum_{n=1}^{\infty} \frac{f(-1)^n}{[(\delta_h/\delta_\lambda)(1-i\gamma_n)-f]} e^{i\theta} e^{-\mu_n \xi}\cos\mu_n z, \quad (18)$$

where the parameter

$$\gamma_n = \frac{E_h \mu_n^3}{(\sigma_h S)^{3/2}} r_T f^2 = \frac{A_h}{f_0 L_d^2}\frac{R_T}{L_d}\mu_n^3, \quad (19)$$

that is, the ratio of the ageostrophic to geostrophic radial velocity in the hydrostatic layer [$\times f^2$, which is $O(1)$]. The solution for the hydrostatic layer follows directly from (17):

$$p_h = -\mathrm{Re} i\tau E_v^{1/2} r_T \frac{\delta_h}{\delta_\lambda} \times \sum_{n=1}^{\infty} \frac{f(-1)^n}{[(\delta_h/\delta_\lambda)(1-i\gamma_n)-f]} e^{i\theta} e^{-\mu_n f \eta}\cos\mu_n z. \quad (20)$$

We focus attention on the pressure anomaly in the wider diffusion layer since it occupies the largest part of the fluid response to the forcing. Note that, if the parameter γ_n were zero so that the radial velocity in the hydrostatic layer were purely geostrophic, the pressure anomaly would be rotated by 90° with respect to the forcing; that is, its azimuthal structure would be proportional to $\sin\theta$. For large values of γ_n the ageostrophic radial velocity dominates, and the pressure anomaly will be in phase with the forcing, that is, possesses a $\cos\theta$ dependence. In most cases the value of γ_1 will be of moderate size, but the higher vertical wavenumbers—the Fourier representations (9) and (13)—forced by the delta function forcing in z will favor the latter structure. The temperature anomaly, which is simply the z derivative of the expressions for the pressure, will share this parametric behavior even more so since larger vertical wavenumbers will contribute more to the temperature. We note from (19) that the larger the island, the more the ageostrophic radial velocity influences the response.

Figure 4 shows the pressure anomaly, near the upper surface, produced around the island by the impinging barotropic flow (4b) and the sink of flow into the upper Ekman layer, for four different values of

$$\gamma_1 = \frac{E_h \pi^3}{(\sigma_h S)^{3/2}} r_T f^2.$$

For reference, if we assume $A_h = 100\ \mathrm{m^2\ s^{-1}}$, $f_0 = 10^{-4}\ \mathrm{s^{-1}}$, $L_d = 30$ km, $R_T = 100$ km, and $\sigma_h = 1$, then $\gamma_1 = 0.11$. For a larger island of radius $R_T = 1000$ km, $\gamma_1 = 1.1$. As γ_1 increases, the ageostrophic radial velocity in the hydrostatic layer increases and, when matched to the geostrophic velocity in the diffusion layer, alters the spatial pattern of the response of the flow until, for large γ_1, in this case $\gamma_1 = 100$, the pattern shifts by 90°. Note also that the (nondimensional) magnitude of the pressure anomaly decreases with increasing γ_1, indicating weaker geostrophic circulation induced around the island. The latter value of γ_1 is probably unrealistically large but it does emphasize the role of the ageostrophic contribution of the radial velocity in the very thin hydrostatic layer on the overall structure of the flow. The ageostrophic contribution is enhanced for larger islands as the rate of change of the pressure along the island's perimeter is reduced. As the stratification increases, the width of the hydrostatic layer increases so the viscous terms, responsible for the ageostrophic radial velocity, decrease. The temperature is just the vertical derivative of the pressure and is easily derived from (20) and shares with the pressure anomaly the sensitivity to the ageostrophic radial velocity in the hydrostatic layer. Both fields change their orientation around the island with depth, rotating as the depth is increased, although the pressure and temperature rotate with depth in opposite directions in the lower range of depth.

Figure 5 shows the contours of temperature (in color) and pressure (white contours) as a function of depth and azimuthal angle at $r = 1.05 r_T$ on the azimuthal range $(-\pi, \pi)$. The pattern is quite similar to that produced by the numerical model in Fig. 3. The maximum temperature anomaly is in the upper ocean but below the surface, while the maximum pressure anomaly is at the surface. There is a similar phase shift between pressure and temperature, and an anticyclonic rotation with depth.

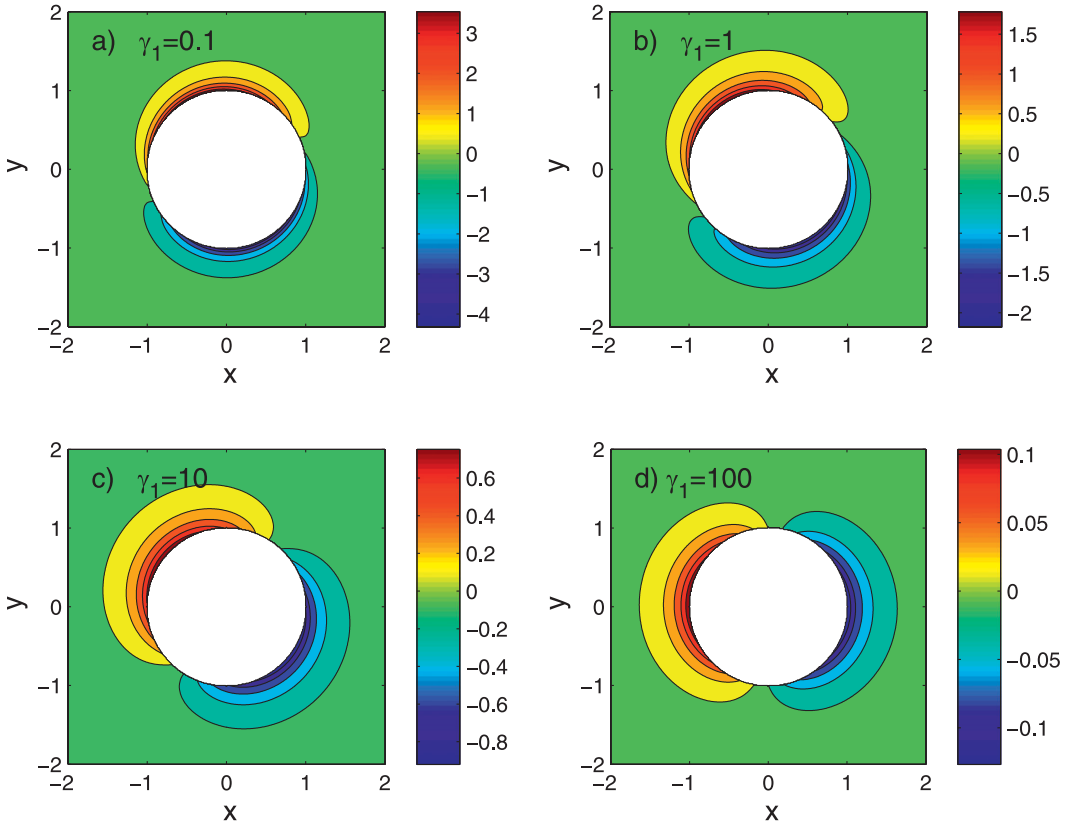

FIG. 4. The pressure anomaly in the relatively broad diffusion layer. (a) For $\gamma_1 = 0.1$ for which the radial velocity in the hydrostatic layer is largely geostrophic. The pressure anomaly is at 90° with respect to the oncoming zonal flow. (b) $\gamma_1 = 1$. Note the alteration in the orientation of the anomaly as the ageostrophic component of the radial velocity in the hydrostatic layer becomes more important. (c) For $\gamma_1 = 10$ and (d) $\gamma_1 = 100$ for which the radial velocity in the hydrostatic layer dominates.

The dynamics of the analytic model explain the regions of vertical mass flux convergence/divergence found in the numerical model. The temperature anomaly is negatively proportional to the vertical velocity. If one integrates across the boundary layer, on the boundary, the temperature gradient perpendicular to the boundary is proportional to the integrated upwelling. Thus, through geostrophy, the vertical gradient of the azimuthal velocity is proportional to the vertical velocity, so the region where the net upwelling is zero will correspond to the crests and troughs in the azimuthal velocity, as in Fig. 3c.

Figure 6 shows the profile of the azimuthal velocity as a function of depth in the diffusion layer near the island (at $r = 1.1r_T$). The flow is purely baroclinic so there is no net azimuthal transport in the boundary layers as was evident from the vertical structure of the forcing in (16). However, the flow structure is very asymmetric in z, reminiscent of the model result in Fig. 3c. A strong flow, very localized near the surface reflecting the concentrated sink of fluid as it enters the upper Ekman layer, is balanced by an oppositely directed flow over the rest of the depth so that the integral is zero. The azimuthal velocity is shown at $\theta = \pi/2$, that is, at the northern extremity of the island. At other angles the velocity has the same structure but reversed with the velocity near the surface flowing in the opposite direction.

3. Topographic effects

The barotropic flow in the interior plays a fundamental role in driving the thermal and hydrostatic boundary layers, and in closing the Ekman layer mass balance at the boundaries. Bottom topography can be very effective at dynamically isolating the island from the barotropic flow in the basin interior through the introduction of regions of closed, diverted, or blocked potential vorticity contours.

a. Topographic slope: Numerical model

The numerical model is configured with topography that slopes uniformly from the island into the basin

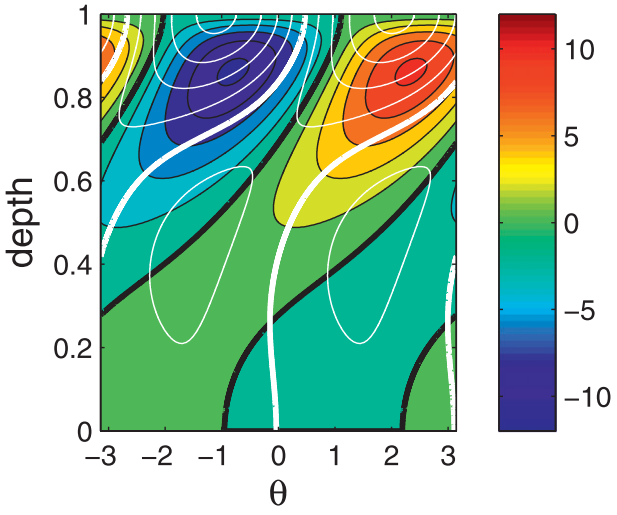

FIG. 5. The isolines of pressure and temperature as a function of z and θ (from $-\pi$ to π) at $r = 1.05r_T$ for the analytic solution.

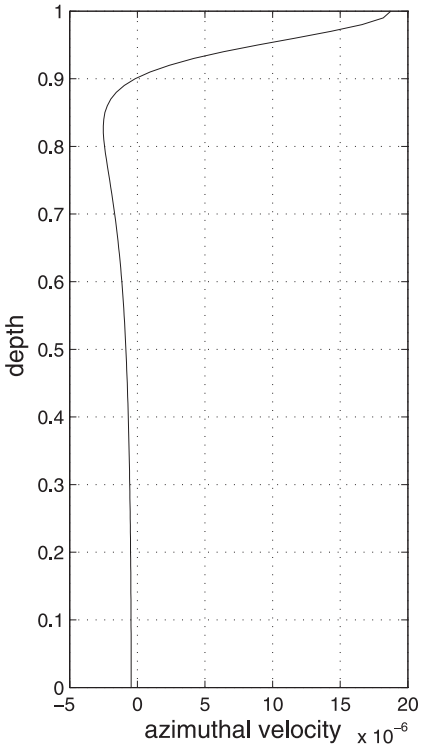

FIG. 6. The profile of azimuthal velocity $v_h(z)$ in the diffusion layer for $\gamma_1 = 0.1$ at $r = 1.1r_T$ and $\theta = \pi/2$.

interior over a width W with slope s. A key parameter $\alpha = fW_s/D\beta R_T$, where R_T is the dimensional radius of the island, measures the relative influence of topography and planetary beta in shaping the barotropic potential vorticity contours, or lines of constant f/h. For $\alpha \gg 1$ the topography overwhelms planetary beta, and the island is surrounded by closed potential vorticity contours. For $\alpha \leq O(1)$ some potential vorticity contours from the basin interior connect the eastern basin to the western basin by passing over the sloping topography equatorward of the island. As we will show, the large-scale circulation resulting from these two limits are quite different. Owing to the expected importance of long Rossby waves, the background restoring time scale has been limited to the regions within 200 km of the outer domain boundaries and decreased to 60 days. The restoring is removed near the island because we are interested in the ability of the approaching barotropic flow to penetrate over the sloping bottom. This requires the development of vertical shear in the velocity, and thus thermal anomalies. Even weak restoring will remove these anomalies and inhibit the ability of the flow to become baroclinic over the sloping bottom. This is not a concern for the flat bottom problem because the baroclinicity is generated at the island, and we expect it to be damped as it penetrates into the stratified interior.

An example of the large α limit is provided by topography that slopes from 25-m depth at the island boundary to 500-m depth over a horizontal distance of $W = 150$ km (slope of $s = 0.0034$, $\alpha = 8$). The barotropic potential vorticity contours are shown in Fig. 7a. Essentially all of the contours around the island are closed. The depth-integrated transport streamfunction is shown in Fig. 7b. The outer edge of the sloping topography is indicated by the white circle. The streamfunction has been scaled by the Ekman transport over the latitude range of the island, so the approaching transport in the Ekman layer in the western shadow of the island is 1. The presence of bottom topography has generated significant depth-integrated recirculation gyres that extend from the western boundary to the eastern side of the island. Recall that the depth-integrated streamfunction for the flat bottom case is zero and that the Ekman transport is uniformly eastward everywhere. The depth-integrated circulation arises because the interior barotropic flow to the east of the island, which was generated by the interaction of the Ekman layer with the eastern boundary, cannot navigate over the sloping topography and so is deflected to the north and south of the island. The Ekman layer on the eastern side of the island is extracting fluid from below the surface very close to the island, which is supplied by flow from the western side of the island. A similar situation arises on the western side of the island, where the fluid downwelling out of the Ekman layer is trapped over the topography and guided eastward to provide the upwelling required of the eastern boundary layers. There is a depth-integrated eastward flow to the west of the island

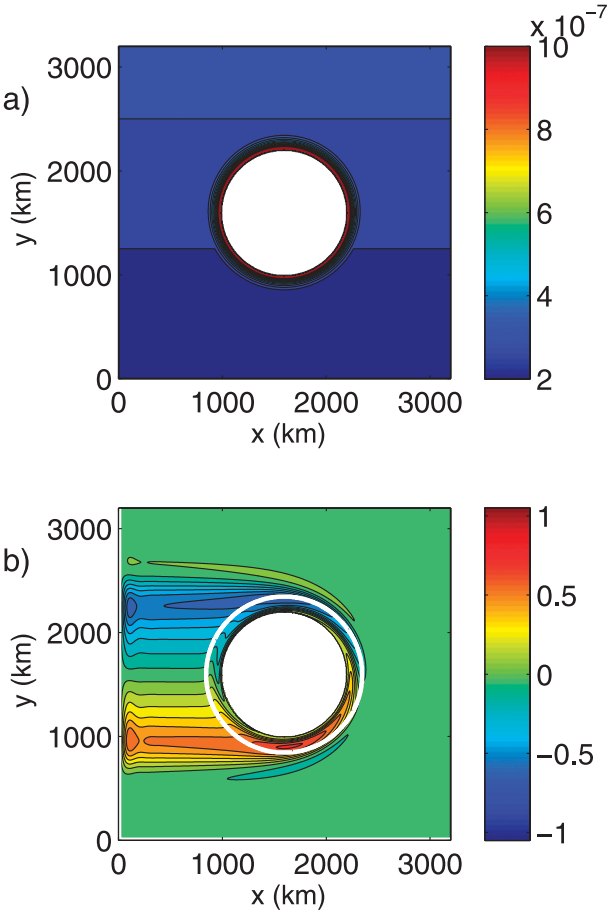

FIG. 7. (a) Barotropic potential vorticity and (b) transport streamfunction for the case with $\alpha = 8$, contour interval 0.1. The white line marks the edge of the sloping topography. The streamfunction is scaled by the eastward Ekman transport directly to the west of the island.

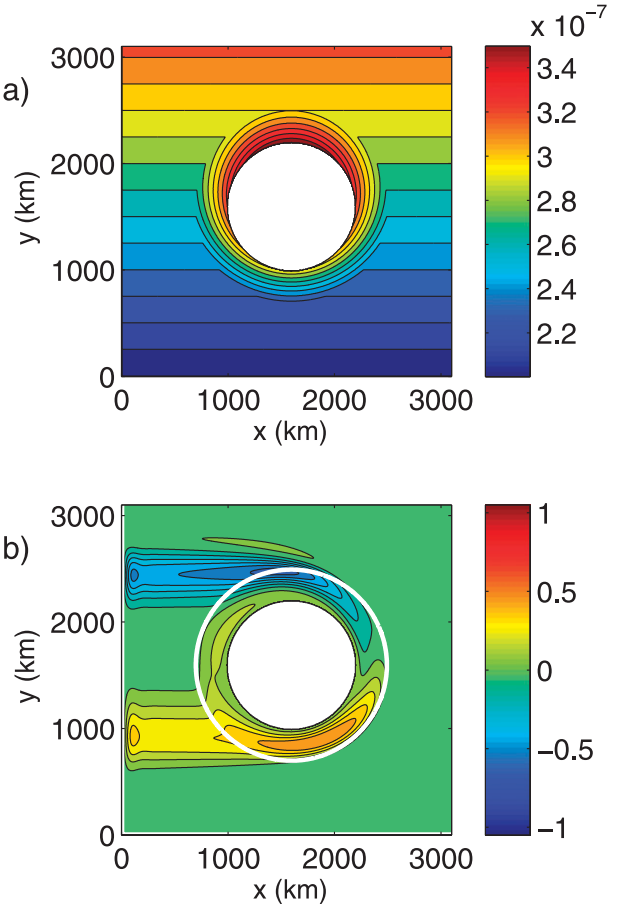

FIG. 8. (a) Barotropic potential vorticity and (b) transport streamfunction for the case with $\alpha = 1.67$, contour interval 0.1. The white line marks the edge of the sloping topography.

approximately equal to the eastward transport in the Ekman layer. The subsurface flow west of the island is near zero because the potential vorticity contours are blocked by the topography around the island. An equivalent mass transport recirculates from the eastern side of the island to the west: this is the diverted barotropic flow that originated on the eastern side of the basin. Although the barotropic transport streamfunction suggests a simple pair of recirculation gyres, the full flow is three-dimensional and quite complex, so individual parcels do not follow such a simple recirculating trajectory.

A case with weaker topography that slopes from 400-m depth on the island boundary to 500-m depth at radius of 900 km ($\alpha = 1.67$) results in a diversion of barotropic potential vorticity contours from the eastern side of the island, around the southern flank over the sloping bottom, and back to the interior to the west of the island (Fig. 8a). Contours to the north of the island over the sloping bottom all intersect the island, producing a region of blocked contours that are isolated from the basin interior. The depth-integrated circulation in this case is much weaker to the west of the island (Fig. 8b). This is because some of the barotropic westward transport to the east of the island follows the potential vorticity contours around the island and into the interior west of the island. Simulated Lagrangian trajectories indicate that parcels approaching the island from the east that are in the lower part of the water column flow around the island and continue to the west. Parcels near the surface flow over the topography and enter the upwelling boundary layer very close to the island. These parcels are transported vertically into the Ekman layer and then returned to the east.

One can infer what will happen if the barotropic return flow that originates at an eastern boundary is blocked somewhere to the east of the island, perhaps by ocean ridges. In this case, the eastward Ekman transport

will interact with the island, the same as previously, but now the mass flux into the Ekman layer along the eastern side of the island must be provided from somewhere to the west. For cases with weak stratification or strong topography, such that there is no communication between the region of closed barotropic potential vorticity contours and the flat interior, this mass flux is provided by water that downwelled out of the Ekman layer along the western side of the island. In these cases the island is very ineffective at blocking the exchange of water from the west of the island to the east of the island. One can imagine a chain of islands separated by small gaps that, in this limit, would be completely permeable to the Ekman transport. In the limit of strong stratification or weak topography, much of the Ekman transport approaching from the west of the island will downwell and return to the west as a barotropic interior flow. In these cases the exchange of the Ekman transport between the region to the west of the island and the region to the east of the island is limited to the Ekman transport that flows directly through the gaps.

b. Topographic slope: Theory

In this section we provide a heuristic calculation to describe one of the most striking consequences of the presence of topography. It is clear that for steep enough topography a portion of the impinging barotropic flow will be diverted by the topography and will tend to follow potential vorticity contours around the skirted part of the island. The extent in the vertical is variable and will depend on the magnitude of the slope and the degree of stratification. We can anticipate that a strongly stratified flow would have its lower portion diverted while the upper strata of the flow would continue to flow toward the island and be entrained into the upper Ekman layer as in the flat bottom calculation of section 2b. However, the volume of fluid locally upwelled into the Ekman layer on the eastern side of the island remains unchanged, as does the flow downwelled on the western side (for a positive meridional wind stress). If the impinging flow is less than the Ekman flux, where does the transport of fluid come from to make up the difference?

We approach that question by using the same model as before except that now, instead of an oncoming barotropic flow (4b), we allow only a fraction F of that flow to impinge on the island so that (4b) is replaced by

$$u_I = -F\frac{\tau}{2f}E_v^{1/2}, \tag{21}$$

where the fraction F will be a free parameter, for this discussion in the range 0 to 1. The former representing a case of low stratification and strong topography when all the flow is steered away from the island by topography, and the latter case is appropriate for the situation in which the topography is weak and the stratification is strong and almost the full barotropic flow impinges on the island as in the previous section. Otherwise, and with a single exception that we discuss below, the analysis is precisely the same as in section 2b.

In the case where the oncoming barotropic flow carried the same transport as the Ekman layer and compensated for it locally, the boundary layers need carry only a purely baroclinic response. That is no longer the case in this model. At the same time, the lower boundary of the region that we are considering needs to be conceived as a level *interior* to the flow and the condition on the density anomaly needs reconsideration. The condition previously used, that the density anomaly vanishes at the lower boundary, would disallow the interior isopycnals to deform. This seems unrealistic and unnecessarily restrictive. We therefore choose to replace the lower boundary condition with the condition of no anomaly of the density gradient, for example,

$$\frac{\partial\rho}{\partial z} = 0, \quad z = 0, \tag{22}$$

so that (10a) and (10b), with the use of (13), remain unchanged except that the series are

$$\hat{u}_{\text{geos}} = -\frac{1}{r_T}\frac{\partial}{\partial\theta}\sum_{n=1}^{\infty}\frac{P_{hn}}{f}e^{-\mu_n f\eta}\sin\mu_n z, \tag{23a}$$

$$\hat{u}_{\text{ageos}} = \frac{E_h\pi^3}{2(\sigma_h S)^{3/2}f}\sum_{n=1}^{\infty} -P_{hn}\mu_n^3 e^{-\mu_n f\eta}\sin\mu_n z, \tag{23b}$$

$$\tilde{u} = -\frac{1}{r_T}\frac{\partial}{\partial\theta}\sum_{n=1}^{\infty}P_{\lambda n}e^{-\mu_n\xi}\sin\mu_n z, \tag{23c}$$

$$\mu_n = (n-1/2)\pi, \tag{23d}$$

which also allows each boundary layer to carry a net *barotropic* transport. The boundary condition (16) becomes

$$-F\frac{E_v^{1/2}}{2f}\tau\cos\theta + U_h\sum_{n=1}^{\infty}\left(-\frac{1}{r_T}\frac{\partial P_{hn}}{\partial\theta} - \frac{E_h\mu_n^3 f}{2\delta_h^3}P_{hn}\right)\sin\mu_n z$$
$$- U_\lambda\sum_{n=1}^{\infty}\frac{1}{fr_T}\frac{\partial P_{\lambda n}}{\partial\theta}\sin\mu_n z = -\frac{\tau}{2f}E_v^{1/2}\cos\theta\delta(z-1), \tag{24}$$

and we note that, for F different from unity, a barotropic response is required. The subsequent analysis is, however, little different than before—leading to the principal

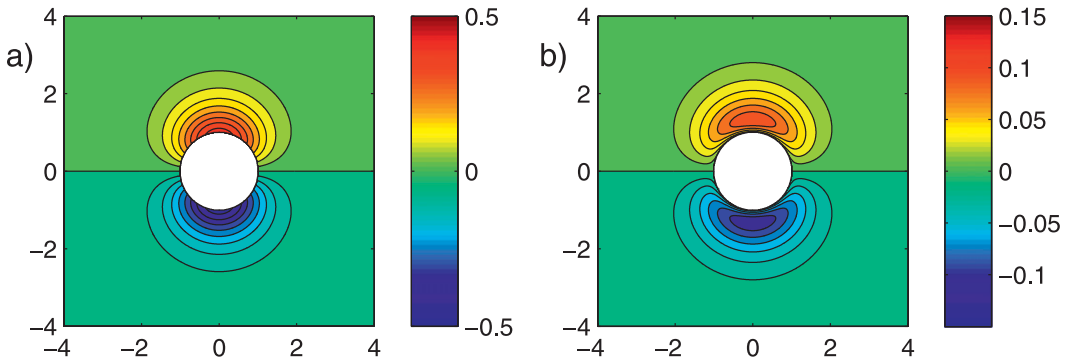

FIG. 9. The barotropic pressure anomaly for the case (a) $F = 0.2$, the geostrophic flow in the diffusion layer exits the hydrostatic layer in the west and enters it on the east to make up the discrepancy between the Ekman flux driven eastward and the oncoming barotropic interior flow, and (b) $F = 1$, a weak barotropic flow occurs although no flow from the diffusion layer enters the hydrostatic layer to be upwelled into the Ekman layer.

result for the amplitude of the flow in the thicker diffusion layer:

$$p_\lambda(\xi,\theta,z) = \mathrm{Re} i\tau E_v^{1/2} r_T \times \sum_{n=1}^{\infty} \frac{f[(-1)^{n+1} - F/\mu_n]}{[(\delta_h/\delta_\lambda)(1-i\gamma_n) - f]} e^{i\theta} e^{-\mu_n \xi} \sin\mu_n z, \tag{25}$$

where the parameter γ_n is given as in (19) except that now we have $\mu_n = (n - 1/2)\pi$. Note that now there is a barotropic pressure field in the diffusion layer given by the integral of (25) between 0 and 1, where we must keep in mind that this is an integral over only the vertical interval in which the fluid is not diverted by topography. The barotropic pressure field is, then,

$$p_{\lambda b}(\xi,\theta,z) = \mathrm{Re} i\tau E_v^{1/2} r_T \times \sum_{n=1}^{\infty} \frac{f[(-1)^{(n+1)} - F/\mu_n](-1)^n}{\mu_n[(\delta_h/\delta_\lambda)(1-i\gamma_n) - f]} e^{i\theta} e^{-\mu_n \xi}. \tag{26}$$

Figure 9a shows the barotropic anomaly in the diffusion layer for the case $F = 0.2$ so that only 20% of the Ekman flux eastward in the upper Ekman layer in the region east of the island can be replaced by the oncoming barotropic flow. The remainder is assumed to have been deflected by the topography and travels to the west on the north and south side of the island. The barotropic pressure shows that the difference is made up for by a flux that has downwelled on the western edge of the island and, in two sweeping gyres, recirculates to enter the upwelling hydrostatic layer on the island's eastern edge. As F increases, which happens when the topography is weaker or when the stratification shields most of the fluid from topographic steering, the net barotropic flow recirculating from the hydrostatic layer on the western side of the island to the eastern side, to subsequently enter the upper Ekman layer, becomes weaker until $F = 1$, when there is no exchange. There is nevertheless a barotropic component to the circulation around the cylinder as shown in Fig. 9b. None of the fluid enters the hydrostatic layer to upwell into the Ekman layer. Note that it is the change in the lower boundary condition from fixed density anomaly to fixed density gradient anomaly that allows for this weak barotropic flow. The deflection of the lowest isopycnal surface is responsible for the appearance of the barotropic circulation.

4. Summary

The interaction between surface Ekman transport forced by a uniform wind stress and circular islands in a stratified ocean has been explored using numerical and analytical models. Despite the different solution techniques and details in configurations, the models give a consistent picture of the complex three-dimensional circulation that results from Ekman transport impinging on an island. Vertical motions are confined to narrow boundary layers, while larger deformation-scale boundary currents also develop in response to the perturbed density field. These baroclinic currents are typically much stronger than the geostrophic flows associated with the Ekman transport alone. Warm (cold) anomalies arise near the surface along the island boundary below downwelling (upwelling) favorable winds. However, these patterns rotate with depth such that the deep ocean can be cold below regions of downwelling and warm below regions of upwelling. The orientation of the pressure anomaly near the island depends on the relative importance of the ageostrophic to geostrophic radial velocity in the hydrostatic layer. The former has a maximum at $\theta = 0$ and π while the latter is greatest

at $\theta = \pm\pi/2$. As the surface is approached, the delta function forcing dominates, the vertical scale of the solution diminishes, and the ageostrophic velocity dominates. The three-dimensional structure of parcel trajectories is quite complex, but for stratified problems it typically enhances the exchange between downwelling and upwelling favorable sides of the island. The addition of a topographic slope around the island produces even more complex flows. The deep flow tends to be along barotropic potential vorticity contours and so avoids the island, but for sufficiently weak topography or strong stratification, the shallow flow can penetrate over the sloping bottom and reach the narrow upwelling/downwelling boundary layers on the island's perimeter. An equivalent transport to that sheared off by the topography, required to balance mass at the base of the Ekman layer, is provided from the base of the Ekman layer elsewhere around the island. Because of this topographically steered communication between upwelling and downwelling boundary layers, the presence of topography makes islands, or island chains, very ineffective at blocking Ekman transport. In contrast to two-dimensional wind-driven coastal upwelling or downwelling, the mass transport into/out of the Ekman layer is provided by flows in the interior of the water column, not within the bottom boundary layer.

Acknowledgments. This study was supported by the National Science Foundation under Grants OCE-0826656 and OCE-0959381 (MAS), and OCE-0925061 (JP). Any opinions, findings, conclusions, or recommendations expressed in this material are those of the authors and do not necessarily reflect the views of the National Science Foundation.

REFERENCES

Allen, J. S., 1973: Upwelling and coastal jets in a continuously stratified ocean. *J. Phys. Oceanogr.,* **3,** 245–257.

——, 1976: Some aspects of the forced wave response of stratified coastal regions. *J. Phys. Oceanogr.,* **6,** 113–119.

Barcilon, V., and J. Pedlosky, 1967: A unified linear theory of homogeneous and stratified rotating fluids. *J. Fluid Mech.,* **29,** 609–621.

Gill, A. E., and A. J. Clarke, 1974: Wind-induced upwelling, coastal currents and sea-level changes. *Deep-Sea Res.,* **21,** 325–345.

Godfrey, J. S., 1989: A Sverdrup model of the depth-integrated flow from the world ocean allowing for island circulations. *Geophys. Astrophys. Fluid Dyn.,* **45,** 89–112.

Lentz, S. J., and D. C. Chapman, 2004: The importance of nonlinear cross-shelf momentum flux during wind-driven coastal upwelling. *J. Phys. Oceanogr.,* **34,** 2444–2457.

Marshall, J., C. Hill, L. Perelman, and A. Adcroft, 1997: Hydrostatic, quasi-hydrostatic, and non-hydrostatic ocean modeling. *J. Geophys. Res.,* **102,** 5733–5752.

Pedlosky, J., 1968: An overlooked aspect of the wind-driven oceanic circulation. *J. Fluid Mech.,* **32,** 809–821.

——, 1974a: On coastal jets and upwelling in bounded basins. *J. Phys. Oceanogr.,* **4,** 3–18.

——, 1974b: Longshore currents, upwelling and bottom topography. *J. Phys. Oceanogr.,* **4,** 214–226.

——, L. J. Pratt, M. A. Spall, and K. R. Helfrich, 1997: Circulation around islands and ridges. *J. Mar. Res.,* **55,** 1199–1251.